Boosting Polysulfide Conversion on Fe-Doped Nickel Diselenide Toward Robust Lithium–Sulfur Batteries

Junshan Li, Jing Yu, Yong Zhang, Canhuang Li, Yi Ma, Huan Ge, Ning Jian, Luming Li, Chao Yue Zhang, Jin Yuan Zhou,* Jordi Arbiol,* and Andreu Cabot**

Sulfur offers a high-energy-density, low-cost, and sustainable alternative to traditional battery cathodes, but its practical use is limited by sluggish and uneven reaction and polysulfide dissolution, necessitating electrocatalytic additives to enhance conversion efficiency. Generating unpaired spin electrons has proven effective in enhancing performance in Co-based electrocatalysts. These unpaired electrons increase polysulfide conversion by enhancing adsorption and weakening S—S bonds, facilitating their cleavage during sulfur reduction reactions. This work extends the strategy to Fe–Ni-based catalysts. The synthesis of $NiSe_2$ and Fe-doped $NiSe_2$ particles is reported and investigate the impact of Fe doping on the electronic structure, catalytic activity, and performance of $NiSe_2$ is introduced as a coating on the cathode side of the Li–S battery (LSB) separator. Experimental analyses and first-principles calculations reveal that Fe-rich cores and surface doping in $NiSe_2$ enhance the density of states at the Fermi level and introduce unpaired electrons, boosting LiPS adsorption and catalytic conversion. These synergistic effects significantly improve the catalytic performance, cycling stability, and overall performance of LSB cells. Specifically, LSB cells based on Fe-doped $NiSe_2$-based separators achieve specific capacities of 1483 mAh g^{-1} at 0.1C and 1085 mAh g^{-1} at 1C, along with remarkable cycling stability, retaining 84.4% capacity after 800 cycles. High sulfur-loading tests further validate the multifunctional membrane's effectiveness, showing significant capacity retention and reduced polysulfide loss.

1. Introduction

Lithium–sulfur batteries (LSBs) are widely regarded as one of the most promising next-generation energy storage technologies due to the abundance and low cost of sulfur as a cathode material, combined with its high theoretical specific capacity (1675 mAh g^{-1}) and energy density (2600 Wh kg^{-1}).[1–6] Despite these advantages, the commercialization of LSBs is hindered by several challenges, including the insulating nature of both the charged (S_8) and discharged (Li_2S) cathode materials and sluggish Li-S reaction kinetics.[7–9] These issues limit charge/discharge rates, reduce the utilization of active material, and impair cycling stability. These challenges are further compounded by active material loss due to lithium polysulfide (LiPS) dissolution and inhomogeneous nucleation of solid phases.[10–12] Furthermore, the migration of LiPSs to the anode causes corrosion and eventual battery failure.

To address the issue of poor electrical conductivity, carbon-based materials are

J. Li, Y. Zhang, Y. Ma, H. Ge, N. Jian, L. Li
Institute for Advanced Study
Chengdu University
Chengdu 610106, China
J. Li, J. Yu, C. Li, A. Cabot
Catalonia Institute for Energy Research – IREC
Sant Adrià de Besòs, Catalonia, Barcelona 08930, Spain
E-mail: canhuangli@irec.cat; acabot@irec.cat

J. Yu, J. Arbiol
Catalan Institute of Nanoscience and Nanotechnology (ICN2)
CSIC and BIST
Campus UAB, Bellaterra, Catalonia, Barcelona 08193, Spain
E-mail: arbiol@icrea.cat
C. Y. Zhang
Department of Chemistry and Biochemistry
University of California
Los Angeles, CA 90095, USA
J. Y. Zhou
School of Physical Science & Technology
Lanzhou University
Lanzhou 730000, China
E-mail: zhoujy@lzu.edu.cn
J. Arbiol, A. Cabot
ICREA
Pg. Lluís Companys 23, Catalonia, Barcelona 08010, Spain

**ADVANCED
SCIENCE NEWS**

www.advancedsciencenews.com
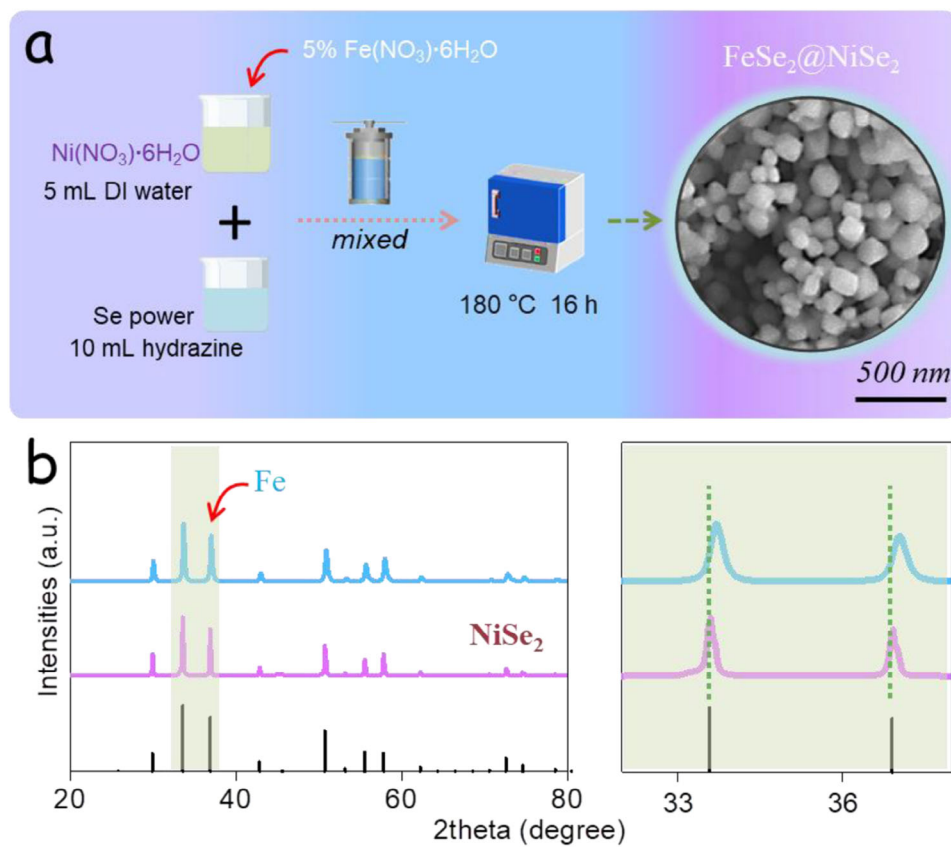
**ADVANCED
FUNCTIONAL
MATERIALS**

www.afm-journal.de

Figure 1. a) Schematic representation of the FeSe$_2$@NiSe$_2$ synthetic procedure and SEM image of the obtained material. b) XRD patterns of NiSe$_2$ and FeSe$_2$@NiSe$_2$ samples.

commonly employed as sulfur hosts.[13] Additionally, the incorporation of additives able to trap LiPSs while simultaneously accelerating their conversion is critical for mitigating their migration and enhancing LSB stability.[14] These additives can be incorporated either into the cathode composite material or applied to the cathode side of the separator. The latter approach simplifies cell manufacturing while delivering comparable or even superior performance.[8,9]

Extensive research has focused on developing efficient catalytic additives for LSBs, particularly those based on 3d transition metal oxides,[2,15–17] nitrides,[18–21] phosphides,[22–24] and chalcogenides.[25–29] Beyond compositional tuning, the performance of these materials can be significantly enhanced through approaches such as doping, heterostructure design, defect engineering, and morphology control to optimize electronic states and promote sulfur redox reactions (SRRs).[30–32]

We, along with others, have demonstrated that generating unpaired spin electrons within Li–S catalysts is an effective strategy to enhance their performance.[33–38] This phenomenon has been investigated using diverse approaches, such as the application of external magnetic fields,[33] the design of heterostructures,[35] and the introduction of atomic vacancies,[34] particularly in Co-based catalysts. The enhanced catalytic activity arises from the increased adsorption of LiPSs, facilitated by the higher density of unpaired electrons generated at the 3d bands of Co.[34] These unpaired electrons not only strengthen the interaction with LiPS

but also weaken the S—S bonds, thereby promoting their cleavage during the sulfur reduction reaction.[33]

In this work, we present a significant advancement in this direction by extending the strategy to cost-effective Fe-Ni-based catalysts synthesized via a simple one-step solution process. Specifically, we report the synthesis of NiSe$_2$ and Fe-doped NiSe$_2$ particles and their introduction as a coated layer on the cathode side of the LSB cell separator. Comprehensive experimental analyses, supported by density functional theory (DFT) calculations, are used to explore the effects of Fe doping on the electronic structure, polysulfide affinity, and catalytic activity of NiSe$_2$, as well as their influence on the cycling stability and overall performance of LSB cells equipped with the modified separators.

2. Results and Discussion

NiSe$_2$ and Fe-modified NiSe$_2$ particles were synthesized using a one-step hydrothermal method, as illustrated in **Figure 1a**. Briefly, aqueous solutions of selenium, nickel, and eventually 5 at% of iron in hydrazine were mixed and hydrothermally processed at 180 °C for 16 h in a sealed autoclave (details provided in the Experimental Section in the Supporting Information, SI). The resulting particles exhibited a quasi-cubic morphology with an average size of 100 ± 30 nm, as observed by scanning electron microscopy (SEM) analysis (Figure 1a; Figure S1,
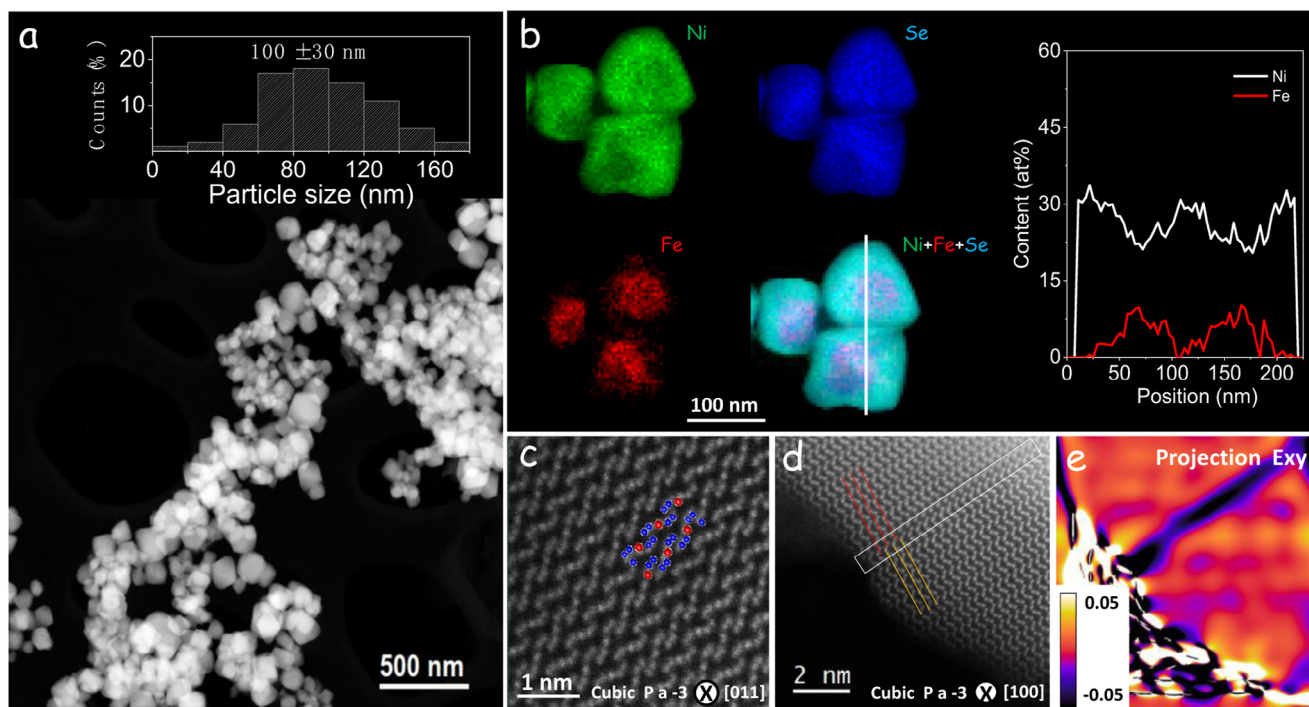
**ADVANCED
SCIENCE NEWS**

www.advancedsciencenews.com

**ADVANCED
FUNCTIONAL
MATERIALS**

www.afm-journal.de

Figure 2. a) HAADF-STEM image of the $FeSe_2$@$NiSe_2$ core-shell nanoparticles and the corresponding particle size histogram. b) EELS-STEM compositional maps (left and middle panel)and the corresponding line scan (right panel). c) Atomic resolution HAADF STEM image along the [011] crystallographic axis showing the BBABB (A = Ni = red, B = Se = blue) atomic arrangement of the $NiSe_2$ shell crystal structure. d) Atomic resolution HAADF STEM image along the [100] crystallographic axis displaying a stacking fault, and e) its corresponding GPA analysis.

Supporting Information). The incorporation of iron did not significantly alter the particle morphology. X-ray diffraction (XRD) analysis confirmed the crystallographic phase of the powders as cubic $NiSe_2$ (JCPDS No. 96-153-7618, Figure 1b).[39] A slight peak shift to higher diffraction angles, indicating lattice contraction, was observed upon the addition of iron.[40–42] No additional peaks were obtained on the Fe-doped sample. Energy dispersive X-ray spectroscopy (EDS) analysis showed the overall composition of the final material to match the nominal amounts of Fe and Ni introduced (Figure S2, Supporting Information).

X-ray photoelectron spectroscopy (XPS) provided further insights into the chemical environments of the elements (Figure S3, Supporting Information). The Ni $2p_{3/2}$ XPS spectrum displays main peaks at 852.7 and 855.1 eV, corresponding to Ni in Ni–Se and Ni–O environments, respectively.[43–45] An additional satellite peak at 860.2 eV is also observed. The Se 3d spectra reveal two doublets, indicative of Se^{2-} in the Ni–Se lattice alongside a Se–O chemical environment. A small amount of Fe was detected at the surface of the particles. The Fe $2p_{3/2}$ spectrum exhibits peaks at 705.9 and 712.1 eV, associated with Fe-Se and Fe–O chemical states, respectively.[42] The introduction of iron caused shifts to lower binding energies in both Ni 2p and Se 3d spectra, suggesting changes in the electronic environment of these elements. The oxygen-based chemical states of Ni, Fe, and Se are likely due to surface oxidation from air exposure during sample preparation for XPS analysis.[46–48] These findings collectively confirm the successful incorporation of iron into the $NiSe_2$ lattice and highlight its influence on the material's structural and electronic properties.

High-angle annular dark-field scanning transmission electron microscopy (HAADF-STEM) analysis confirmed the quasi-cubic morphology and size of the particles (**Figure 2a**). Electron energy loss spectroscopy (EELS) elemental mapping revealed a distinct core-shell architecture, with a Fe-rich core surrounded by a $NiSe_2$ shell (Figure 2b left and middle panels). Line scans illustrate the variation in metal ratios across two particles shown in Figure 2b right panel, while a more intuitive 2D elemental distribution is presented in Figure S4 (Supporting Information). The core size and shell thickness are estimated at ≈40 and 30 nm, respectively. Near the particle surface, the Ni ratio is close to 1, indicating a minor Fe concentration in the shell, and decreases to ≈0.68 toward the core. Assuming all the Fe is concentrated within the particle core, the introduced Fe atomic ratio (Ni/Fe = 19) corresponds to a pure $FeSe_2$ core with an estimated size of ≈37 nm within a 100 nm particle. This configuration would result in a calculated Ni concentration of ≈0.63. These estimations are consistent with the dimensions and Ni concentration observed in the electron microscopy analysis, suggesting that the core predominantly consists of $FeSe_2$ with minor Ni incorporation.

Detailed structural analysis of the cubic $NiSe_2$ phase, viewed along the [011] crystallographic axis (Figure 2c), revealed a BBABB (A = Ni, B = Se) atomic arrangement. Although selenium has a slightly higher atomic number, the Ni atomic columns appear brighter in HAADF STEM images due to their higher atomic density. To investigate the influence of Fe doping on the crystal structure, geometric phase analysis (GPA) was performed on HAADF STEM images viewed along the [100] crystallographic axis (Figure 2d,e; Figure S5, Supporting Information). This
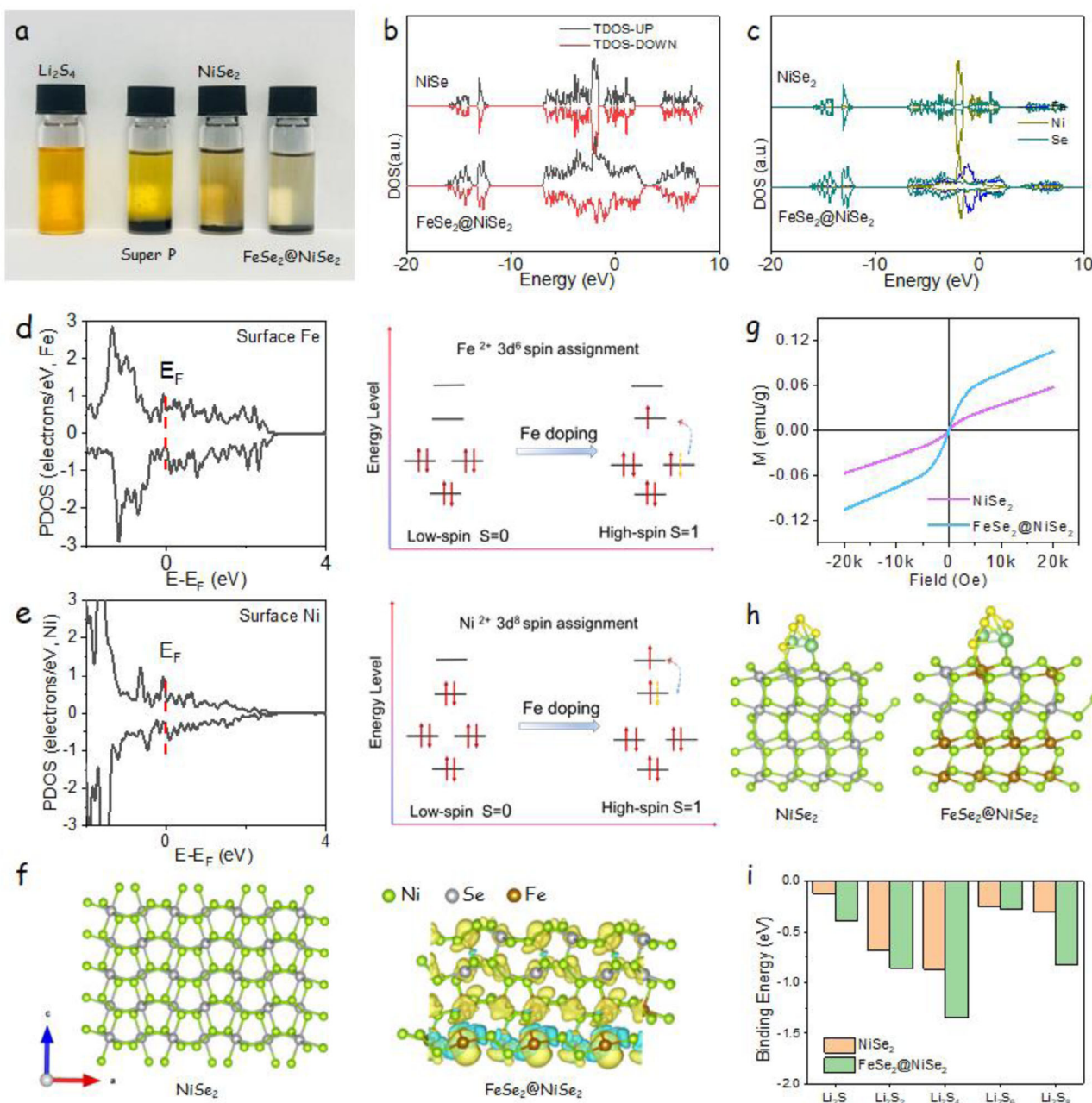
2501485 (3 of 9)

**ADVANCED
SCIENCE NEWS**

www.advancedsciencenews.com

**ADVANCED
FUNCTIONAL
MATERIALS**

www.afm-journal.de

Figure 3. a) Optical images of the polysulfide solutions after overnight interaction with different adsorbents. b,c) DOS and PDOS of NiSe$_2$ and FeSe$_2$@NiSe$_2$. d,e) Spin polarization for surface Fe and Ni. f) Spin density of NiSe$_2$ and FeSe$_2$@NiSe$_2$. Yellow = spin-up and blue = spin-down. The isosurface level of spin density is 0.001 e/a$_0^3$. g) M–H curve of NiSe$_2$ and FeSe$_2$@NiSe$_2$ particles at room temperature. h,i) Relaxed Li$_2$S$_6$-adsorbed structures on the surface of NiSe$_2$ and FeSe$_2$@NiSe$_2$. Brown = Fe; Grey = Ni; Green = Se.

analysis highlighted the presence of stacking faults, likely introduced by structural defects during crystal growth.

Li$_2$S$_4$ adsorption experiments were conducted to assess the LiPS trapping capabilities of the NiSe$_2$ and FeSe$_2$@NiSe$_2$ particles. Equal amounts of each material were introduced into 5 mM Li$_2$S$_6$ solutions and left undisturbed overnight. A high-conductivity carbon material, Super P, was also tested as a reference. After the adsorption period, optical images (**Figure 3**a) revealed that the Li$_2$S$_4$ solution retained a deep orange color,

while the solutions containing NiSe$_2$ and Super P exhibited a lighter yellowish color, and the solution containing FeSe$_2$@NiSe$_2$ was nearly transparent. Further evidence of the reduced LiPS concentration in solution was provided by UV-vis spectroscopy (Figure S6, Supporting Information). The characteristic absorption band of Li$_2$S$_4$ observed between 350 nm and 400 nm, was notably diminished in the presence of the adsorbent materials. Most prominently, the solution containing FeSe$_2$@NiSe$_2$ exhibited minimal UV-vis absorption peaks, indicating a strong adsorption

capacity that effectively removed Li_2S_4 from the solution. These findings highlight the superior performance of $FeSe_2@NiSe_2$ in polysulfide adsorption, suggesting that the $FeSe_2$ core and Fe doping enhance the interaction of the $NiSe_2$ surface with polysulfides.[49]

Figure S7 (Supporting Information) presents the Ni 2p, Se 3d, and Fe 2p XPS spectra of $NiSe_2$ and $FeSe_2@NiSe_2$ after the LiPS adsorption tests. The spectra for each element exhibit two distinct contributions: one corresponding to the lattice environment and another to a surface oxidized state. Notably, all the spectra show a slight shift following LiPS adsorption, as compared to the data in Figure S3 (Supporting Information). This shift is attributed to the interaction between the catalyst's surface sites and Li_2S_4, reorganizing electronic density.[50]

DFT calculations were used to analyze the electronic structure of the material and its influence on the interaction between the host materials and LiPSs.[51–53] The presence of Fe introduces a large density of states (DOS) at the Fermi level (Figure 3b,c). Quantitively, the d-band center of the $FeSe_2@NiSe_2$ is calculated to be at −0.556 eV, closer to the Fermi level compared to $NiSe_2$ (−1.035 eV). This shift increases the probability of electrons filling the antibonding orbital, thereby enhancing the adsorption of LiPSs and promoting the deposition of Li_2S.[15,54] In parallel, the presence of Fe introduces a significant asymmetry in the electron spin configuration, as seen in Figure 3d,e, resulting in up to 24% increase in spin polarization at surface metal sites. Figure 3f further illustrates the enhanced density of unpaired electrons due to Fe incorporation and their localization. This result is corroborated by magnetization measurements at room temperature, which reveal that Fe addition significantly increases the material's magnetization (Figure 3g). This result is consistent with the weaker Ni satellite peaks observed in the XPS spectra of $FeSe_2@NiSe_2$ compared to $NiSe_2$ that also suggests higher magnetic susceptibility in the $FeSe_2@NiSe_2$ system (Figure S3, Supporting Information).

Figure 3h shows the Li_2S_6 adsorption configuration on a pure $NiSe_2$ surface and a Fe-doped $NiSe_2$ surface grown over $FeSe_2$. The DFT results revealed that the Li_2S, Li_2S_2, Li_2S_4, Li_2S_6, and Li_2S_8 binding energy on the $FeSe_2@NiSe_2$ is higher than that of $NiSe_2$ (Figure 3h,i). Specifically, the adsorption energies of Li_2S, Li_2S_2, Li_2S_4, Li_2S_6 and Li_2S_8 on $FeSe_2@NiSe_2$ were calculated at −0.393, −0.859, −1.344, −0.279, and −0.821 eV, which are significantly larger than the values obtained on the $NiSe_2$ surface (−0.119, −0.686, −0.871, −0.252, and −0.252 eV).

To assess the electrocatalytic activity toward the conversion of polysulfides, symmetric cells containing 0.5 M Li_2S_6 electrolyte were assembled and tested using cyclic voltammetry (CV) in the voltage range of -1 to 1 V. As can be seen in **Figure** 4a, the symmetric cell based on $FeSe_2@NiSe_2$ electrodes exhibited larger current densities, indicating a higher electrochemical activity for the conversion of polysulfides.

Subsequently, coin-type cells based on a S@Super P cathode, a Li anode, and a polypropylene (PP) membrane coated with the $NiSe_2$ or $FeSe_2@NiSe_2$ catalyst at the cathode side as the separator were assembled and tested (see details in the SI and Figure S8, Supporting Information). Figure 4b shows the galvanostatic charge-discharge (GCD) profiles under a constant current of the $NiSe_2$/PP and $FeSe_2@NiSe_2$/PP cells and a reference cell with an uncoated PP separator, thus containing no catalyst. GCD profiles

display one charge plateau and two distinct discharge plateaus. The first discharge plateau, from 2.4 to 2.1 V, yields a capacity Q1, which corresponds to the reduction of S_8 to Li_2S_4 ($S_8 + 4Li^+ + 4e^- \rightarrow 2Li_2S_4$). The second discharge plateau, occurring between 2.1 and 1.7 V, yields capacity Q_2 and is associated with the reduction of Li_2S_4 to insoluble lithium sulfide ($2Li_2S_4 + 12Li^+ + 12e^- \rightarrow 8Li_2S$). As displayed in Figure 3b, the $FeSe_2@NiSe_2$/PP cell exhibited a discharge capacity of 1484 mAh g^{-1}, which is well above the capacities of the $NiSe_2$/PP cell at 1186 mAh g^{-1} and that of the catalyst-free cell at 885 mAh g^{-1}.

The potential difference, ΔE, between the charge and discharge curves at 50% of the discharge capacity is commonly defined as the polarization potential of the LSBs.[55–57] This metric provides a quantitative assessment of the LiPS conversion kinetics. The cell with the $FeSe_2@NiSe_2$/PP separator exhibited a reduced polarization voltage of $\Delta E = 150$ mV, which is lower than that observed for cells with the $NiSe_2$/PP ($\Delta E = 160$ mV) and PP ($\Delta E = 168$ mV) separators (Figure 4c).

The electrocatalytic performance of the catalysts was further evaluated by analyzing the capacity ratio between the two reduction plateaus, Q_2/Q_1. Ideally, this ratio should approach 3, as Q_1 corresponds to a 4-electron reduction reaction and Q_2 to a 12-electron reduction reaction.[58–60] However, in practical applications, lower Q_2/Q_1 ratios are commonly observed due to the incomplete reduction of Li_2S, often resulting in the formation of partially discharged Li_2S_2 products and the migration of LiPSs to the negative electrode. This reduces the active material available at the cathode. As shown in Figure 4c, cells with $FeSe_2@NiSe_2$/PP separators achieved an exceptionally high Q_2/Q_1 ratio of 2.6, surpassing those with $NiSe_2$/PP separators (2.4) and catalyst-free PP separators (2.1). These findings demonstrate that the presence of Fe significantly enhances the redox kinetics of the Li–S reaction.

To gain deeper insights into the electrochemical processes during battery cycling, the CV curves of the assembled cells are presented in Figure 4d. Each curve features a single oxidation peak (Peak III) and two reduction peaks (Peaks I and II), corresponding to the S to Li_2S conversion reactions, consistent with the charge-discharge profiles.[61] A comparison of the two cells reveals that the one utilizing the $FeSe_2@NiSe$/PP separator exhibits the highest peak current density and the most pronounced onset potentials for both reduction and oxidation (Figure 4d,e). These observations align with the polarization voltage results, highlighting the superior electrocatalytic performance of the $FeSe_2@NiSe_2$/PP separator.

As the scan rate increases from 0.1 to 0.4 mV s^{-1} (Figure 4f; Figure S9, Supporting Information), the reduction peaks shift to more negative potentials, while the oxidation peak shifts to more positive potentials, reflecting an increase in polarization voltage. Notably, cells equipped with $FeSe_2@NiSe_2$/PP separators exhibit significantly higher current densities and reduced polarization voltage compared to their counterparts in the entire scan rate range. The linear relationship observed between the peak current and the square root of the scan rate indicates that the reactions are diffusion-controlled. This behavior allows the estimation of the lithium-ion (Li$^+$) diffusion coefficient using the Randles–Ševčík equation:[62]

$$I_p = \left(2.69 * 10^5\right) n^{1.5} A D_{Li^+}^{0.5} C_{Li^+} \nu^{0.5} \tag{1}$$

2501485 (5 of 9)

**ADVANCED
SCIENCE NEWS**

www.advancedsciencenews.com

**ADVANCED
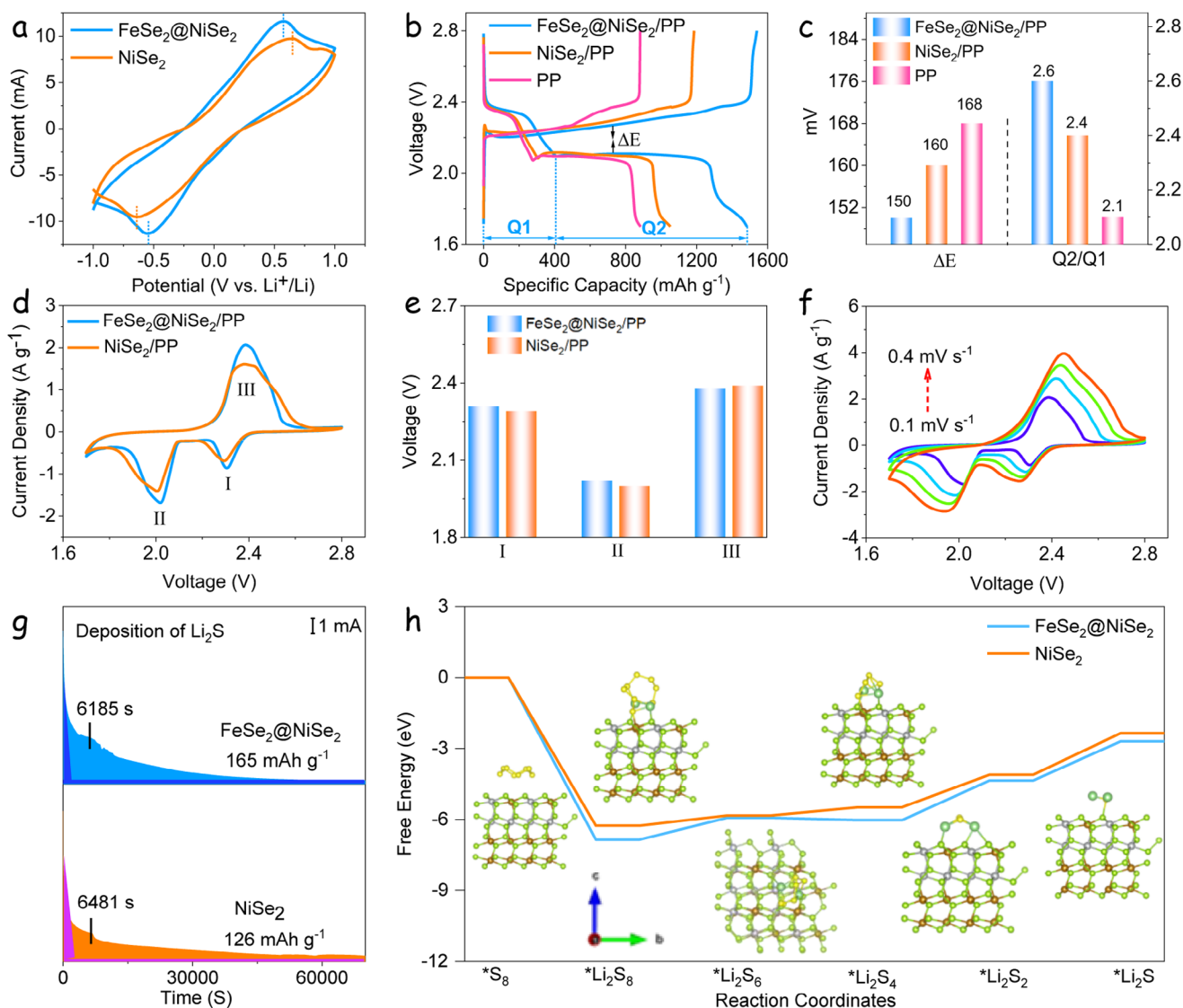FUNCTIONAL
MATERIALS**

www.afm-journal.de

Figure 4. a) CV profiles of symmetrical cells with NiSe$_2$ and FeSe$_2$@NiSe$_2$ electrodes using an electrolyte containing 0.5 M Li$_2$S$_6$ and 1 M LiTFSI dissolved in DOL/DME (v/v = 1/1). b) GCD profiles of cells based on NiSe$_2$/PP or FeSe$_2$@NiSe$_2$/PP separators at the current rate of 0.1 C. c) ΔE and Q2/Q1 values derived from GCD profiles. d) CV profiles of Li-S coin cells with different separators. e) Peak voltages obtained from CV curves with different separators. f) CV curves of FeSe$_2$@NiSe$_2$/PP cells at various scan rates from 0.1 to 0.4 mV s^{-1}. g) Potentiostatic discharge profile of Li$_2$S nucleation at 2.05 V on different materials with Li$_2$S$_8$ catholyte. h) Relative energy distribution of various reacting species along the reaction pathway on the NiSe$_2$ and FeSe$_2$@NiSe$_2$ surface.

where I_p is the peak current, n is the number of electrons transferred, A is the electrode's area, D_{Li}^+ is the Li$^+$ diffusion coefficient, C_{Li}^+ is the Li$^+$ concentration in the electrolyte, and ν is the scan rate.

Figure 4f shows that cells with FeSe$_2$@NiSe$_2$/PP membranes have the steepest slopes across all three reaction peaks, indicating the highest Li$^+$ diffusion rate. As shown in Figure S10 (Supporting Information), for Peaks I, II, and III, the Li$^+$ diffusion coefficients in FeSe$_2$@NiSe$_2$/PP cells are 7.2 × 10^{-7}, 2.5 × 10^{-7}, and 4.5 × 10^{-7} cm^2 s^{-1}, substantially higher than those for NiSe$_2$/PP cells (5.7 × 10^{-7}, 2.2 × 10^{-7}, and 4.0 × 10^{-7} cm^2 s^{-1}). These are related to the electrolyte viscosity, which increases with LiPS accumulation, and the formation of insulating Li$_2$S/Li$_2$S$_2$

layers on electrodes, both strongly affecting Li$^+$ diffusivity.[63] The higher diffusion coefficients observed in FeSe$_2$@NiSe$_2$/PP cells further confirm that iron presence enhances the Li–S reaction and effectively traps LiPS.

Li$_2$S deposition experiments were used as an additional quantitative measure of the catalytic activity of different active materials.[57] In this case, FeSe$_2$@NiSe$_2$ and NiSe$_2$ were tested as electrode materials (see details in the SI). The FeSe$_2$@NiSe$_2$-based electrode exhibits a higher current response during constant potential polarization at 2.05 V, as shown in Figure 4g. According to Faraday's law ($Q = I t$, where Q, I, and t represent capacity, discharge current, and time, respectively),[64] the deposition capacity of FeSe$_2$@NiSe$_2$ (165 mAh g^{-1}) is significantly
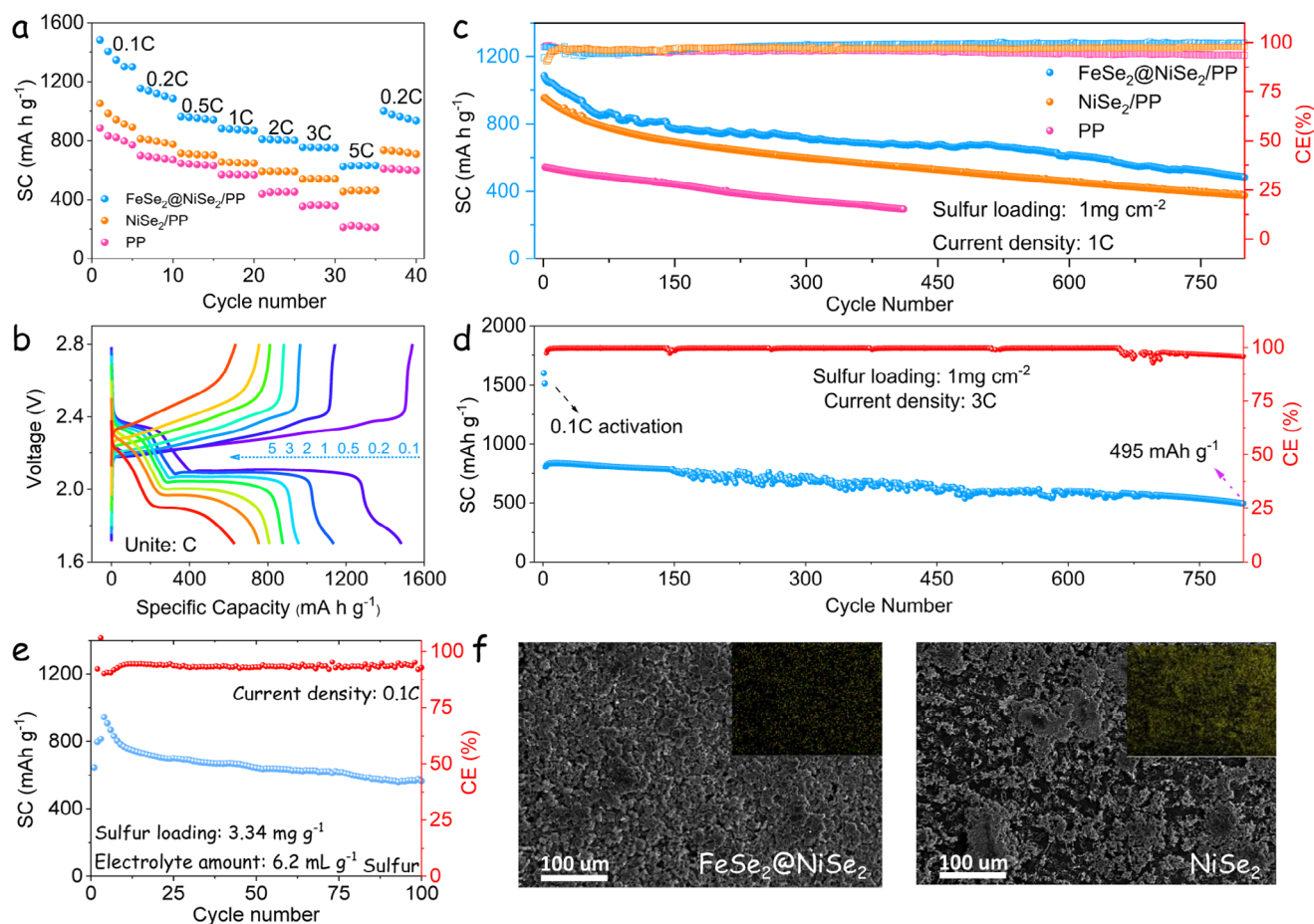
ADVANCED
SCIENCE NEWS

www.advancedsciencenews.com

ADVANCED
FUNCTIONAL
MATERIALS

www.afm-journal.de

Figure 5. a,b) Rate performances of PP, $NiSe_2$/PP, and $FeSe_2@NiSe_2$/PP cells. b) GCD curves of $FeSe_2@NiSe_2$/PP cells at current rates from 0.1 to 5C c) Capacity retention of PP, $NiSe_2$/PP, and $FeSe_2@NiSe_2$/PP cells at 1C over 800 cycles. d) Cycling stability of $FeSe_2@NiSe_2$/PP cell at 3C over 800 cycles. e) Cycling stability of a $FeSe_2@NiSe_2$/PP cell with high sulfur loading and lean electrolyte conditions. f) SEM image and EDS of lithium foil disassembled from a coin cell based on $NiSe_2$/PP and $FeSe_2@NiSe_2$/PP separators.

larger than that of $NiSe_2$ (126 mAh g^{-1}). Thus, nucleation experiments also indicate that the Fe presence effectively reduces the reaction barrier for Li_2S nucleation, thereby promoting the complete conversion of LiPS.

DFT calculations were further used to compare the Gibbs free energy evolution of the sulfur reduction reaction on the surface of $FeSe_2@NiSe_2$ and $NiSe_2$. The optimized model and free energy distribution of polysulfide intermediates are shown in Figure 4h. The first step of the sulfur lithiation pathway is the reaction of two Li$^+$ with S_8 to form Li_2S_8, followed by a subsequent reduction to Li_2S_6, Li_2S_4, Li_2S_2, and finally Li_2S. As can be seen from the first step, the formation of Li_2S_8 was enhanced with the presence of Fe. Besides, the energy barrier for the rate-limiting step, the conversion of Li_2S_2 to Li_2S was lower for $FeSe_2@NiSe_2$, at 1.66 eV, than for $NiSe_2$, at 1.76 eV.

Figure 5a displays the rate performance of cells based on $FeSe_2@NiSe_2$/PP and $NiSe_2$/PP separators in the current density range of 0.1C to 5C. $FeSe_2@NiSe_2$/PP cells consistently exhibit the highest discharge-specific capacities. Notably, $FeSe_2@NiSe_2$/PP cells display a remarkable capacity of 1483 mAh g^{-1} in the initial discharge at 0.1C and maintain a high specific capacity up 1154, 963, 880, 810, 754, and 624 mAh g^{-1} at

0.2C, 0.5C, 1.0C, 2.0C, 3.0C, and 5.0C (Figure 5b), higher than that obtained from the $NiSe_2$ and catalyst-free cells (Figure S11, Supporting Information). When the current rate is set to 0.2C again, the cell still delivers a substantial specific capacity of 1000 mAh g^{-1}, demonstrating excellent stability. The electrochemical cycling performance of the pure catalysts shows it does not contribute to the capacity, with no additional voltage plateau appearing during the battery cycling in Figure S12 (Supporting Information). Also, the XRD patterns of the separator before and after the rate cycling (Figure S13, Supporting Information) confirm that the catalyst was stable during the electrochemical process, without phase change or generation of additional phases.

Figure 5c displays the cycling performance of different electrodes at a 1C current rate. The $FeSe_2@NiSe_2$/PP cell exhibits the highest capacity over continuous 800 cycles. Specifically, it has an initial discharge capacity of ≈1085 mAh g^{-1} at 1C, and it retains 84.4% of its initial capacity after 800 cycles. The decay in cycling performance is similar to the $NiSe_2$-based cell. Thus, we selected the $FeSe_2@NiSe_2$/PP multifunctional separator to assess its cycling performance at 3C. As shown in Figure 5d, after a few initial activation cycles at 0.1C, the $FeSe_2@NiSe_2$/PP cell delivers a discharge specific capacity of 1613 mAh g^{-1}, and even after 800

**ADVANCED
SCIENCE NEWS**

www.advancedsciencenews.com

**ADVANCED
FUNCTIONAL
MATERIALS**

www.afm-journal.de

cycles, the specific capacity was found to be 495 mAh g^{-1}, corresponding to an average decay rate of 0.55% per cycle.

To achieve the high energy density needed for practical applications, increasing the sulfur loading is essential. Consequently, a series of electrochemical tests were performed on cells equipped with a FeSe$_2$@NiSe$_2$/PP membrane under high sulfur loading conditions (3.34 mg g^{-1}). Figure 5e displays the cycling performance, which demonstrates an initial discharge capacity of 940 mAh g^{-1} at 0.1C, stabilizing after over 100 continuous cycles at 564 mAh g^{-1}.

SEM characterization revealed a rough and cracked surface on the lithium metal recovered from the NiSe$_2$-based cell, attributed to lithium dendrite growth and LiPS-related corrosion. In contrast, the lithium metal electrode retrieved from the FeSe$_2$@NiSe$_2$/PP cell showed a smooth, even surface with minimal cracks. Subsequent EDX compositional mapping indicated significantly lower sulfur content on the Li foil recovered from the FeSe$_2$@NiSe$_2$/PP cell compared to the lithium foil extracted from the NiSe$_2$ cell, as shown in Figure 5f.

3. Conclusion

In summary, we successfully synthesized Fe-doped NiSe$_2$ particles containing a Fe-rich core via a one-step hydrothermal method and investigated their application as electrocatalysts on the cathode side of a PP separator in LSBs. Electrochemical performance tests demonstrated that FeSe$_2$@NiSe$_2$/PP cells achieved outstanding rate capabilities and cycling stability, with specific capacities of 1483 mAh g^{-1} at 0.1C and 1085 mAh g^{-1} at 1C. Remarkably, the cells retained 84.4% of their capacity after 800 cycles, highlighting their long-term durability. Even under high sulfur loading, the electrode exhibited excellent capacities and stable cycling performance. DFT calculations revealed that the substantial DOS at the Fermi level, coupled with the additional unpaired electrons generated by the Fe-rich core and Fe doping on the NiSe$_2$ surface, significantly enhanced the binding affinity for LiPSs. This, in turn, facilitated efficient sulfur redox reactions, accelerating the Li-S reaction kinetics. The increased binding energies for LiPSs due to Fe doping were also confirmed, further validating its role in improving catalytic activity. This study highlights the potential of Fe-activated NiSe$_2$ particles as robust electrocatalysts for LSBs, offering a promising pathway toward the development of next-generation energy storage technologies.

Supporting Information

Supporting Information is available from the Wiley Online Library or from the author.

Conflict of Interest

The authors declare no conflict of interest.

Data Availability Statement

The data that support the findings of this study are available in the supplementary material of this article.

[1] M. Zhao, B. Q. Li, X. Q. Zhang, J. Q. Huang, Q. Zhang, *ACS Cent. Sci.* **2020**, *6*, 1095.

[2] X. Liu, J. Q. Huang, Q. Zhang, L. Mai, *Adv. Mater.* **2017**, *29*, 1601759.

[3] D. Yang, C. Li, M. Sharma, M. Li, J. Wang, J. Wei, K. Liu, Y. Zhang, J. Li, G. Henkelman, Q. Zhang, A. Cabot, *Energy Storage Mater.* **2024**, *66*, 103240.

[4] W. Bi, C. Li, D. Yang, Y. Z. Zhang, L. Hu, Q. Gong, J. Zhang, Y. Zhang, M. Li, J. Wei, Y. Zhou, D. Zhou, T. Wu, L. F. Chen, A. Cabot, *Energy Environ. Sci.* **2025**, *18*, 1929.

[5] J. Xiang, Y. Qu, Y. Zeng, S. Hu, H. Xu, H. Xia, M. Ji, L. Duan, F. Lu, *Energy Mater. Adv.* **2023**, *4*, https://doi.org/10.34133/energymatadv.0054.

[6] M. Jana, R. Xu, X. B. Cheng, J. S. Yeon, J. M. Park, J. Q. Huang, Q. Zhang, H. S. Park, *Energy Environ. Sci.* **2020**, *13*, 1049.

[7] Y. Jin, N. Deng, Y. Li, H. Wang, M. Zhang, W. Kang, B. Cheng, *J. Energy Chem.* **2024**, *88*, 469.

[8] C. Li, D. Yang, J. Yu, J. Wang, C. Zhang, T. Yang, C. Huang, B. Nan, J. Li, J. Arbiol, Y. Zhou, Q. Zhang, A. Cabot, *Adv. Energy Mater.* **2024**, *14*, 2303551.

[9] C. Li, J. Yu, C. Zhang, D. Yang, J. Wang, H. Li, C. Huang, K. Xiao, Y. Cheng, Y. Ren, X. Qi, T. Yang, J. Li, J. Wang, G. Henkelman, J. Arbiol, J. Nan, A. Cabot, *J. Colloid Interface Sci.* **2024**, *670*, 61.

[10] T.-C. Liu, *J. Electrochem. Soc.* **1998**, *145*, 1882.

[11] J. Shin, W.-H. Ryu, K.-S. Park, I.-D. Kim, *ACS Nano* **2013**, *7*, 7330.

[12] J. Feng, C. Shi, H. Dong, C. Zhang, W. Liu, Y. Liu, T. Wang, X. Zhao, S. Chen, J. Song, *J. Energy Chem.* **2023**, *86*, 135.

[13] S. Evers, L. F. Nazar, *Acc. Chem. Res.* **2013**, *46*, 1135.

[14] J. Q. Huang, Q. Zhang, S. M. Zhang, X. F. Liu, W. Zhu, W. Z. Qian, F. Wei, *Carbon* **2013**, *58*, 99.

[15] J. Liu, L. Yu, Q. Ran, X. Chen, X. Wang, X. He, H. Jin, T. Chen, J. S. Chen, D. Guo, S. Wang, *Small* **2024**, *20*, 2311750.

[16] X. Song, G. Chen, S. Wang, Y. Huang, Z. Jiang, L. X. Ding, H. Wang, *ACS Appl. Mater. Interfaces* **2018**, *10*, 26274.

[17] D. Zhang, T. Duan, Y. Luo, S. Liu, W. Zhang, Y. He, K. Zhu, L. Huang, Y. Yang, R. Yu, X. Yang, H. Shu, Y. Pei, X. Wang, M. Chen, *Adv. Funct. Mater.* **2023**, *33*, 2306578.

[18] T. Zhu, Y. Sha, H. Zhang, Y. Huang, X. Gao, M. Ling, Z. Lin, *ACS Appl. Mater. Interfaces* **2021**, *13*, 20153.

[19] Z. Cheng, Y. Wang, W. Zhang, M. Xu, *ACS Appl. Energy Mater.* **2020**, *3*, 4523.

[20] L. Ma, H. Yuan, W. Zhang, G. Zhu, Y. Wang, Y. Hu, P. Zhao, R. Chen, T. Chen, J. Liu, Z. Hu, Z. Jin, *Nano Lett.* **2017**, *17*, 7839.

[21] W. Sun, Z. Song, Z. Feng, Y. Huang, Z. J. Xu, Y. C. Lu, Q. Zou, *Nano-Micro Lett.* **2022**, *14*, 222.

[22] Y. Zhong, L. Yin, P. He, W. Liu, Z. Wu, H. Wang, *J. Am. Chem. Soc.* **2018**, *140*, 1455.

[23] W. Song, X. Yang, T. Zhang, Z. Huang, H. Wang, J. Sun, Y. Xu, J. Ding, W. Hu, *Nat. Commun.* **2024**, *15*, 1005.

[24] Y. Chen, W. Zhang, D. Zhou, H. Tian, D. Su, C. Wang, D. Stockdale, F. Kang, B. Li, G. Wang, *ACS Nano* **2019**, *13*, 4731.

[25] W. Yao, W. Zheng, J. Xu, C. Tian, K. Han, W. Sun, S. Xiao, *ACS Nano* **2021**, *15*, 7114.

[26] T. Sun, C. Huang, H. Shu, L. Luo, Q. Liang, M. Chen, J. Su, X. Wang, *ACS Appl. Mater. Interfaces* **2020**, *12*, 57975.

[27] H. Lin, L. Yang, X. Jiang, G. Li, T. Zhang, Q. Yao, G. W. Zheng, J. Y. Lee, *Energy Environ. Sci.* **2017**, *10*, 1476.

[28] R. Lv, J. A. Robinson, R. E. Schaak, D. Sun, Y. Sun, T. E. Mallouk, M. Terrones, *Acc. Chem. Res.* **2015**, *48*, 56.

[29] D. Yang, M. Li, X. Zheng, X. Han, C. Zhang, J. Jacas Biendicho, J. Llorca, J. Wang, H. Hao, J. Li, G. Henkelman, J. Arbiol, J. R. Morante, D. Mitlin, S. Chou, A. Cabot, *ACS Nano* **2022**, *16*, 11102.

[30] J. S. Yeon, Y. H. Ko, T. H. Park, H. Park, J. Kim, H. S. Park, *Energy Environ. Mater.* **2022**, *5*, 555.

[31] S. S. Chen, Z. Z. Yang, A. J. Wang, K. M. Fang, J. J. Feng, *J. Colloid Interface Sci.* **2018**, *509*, 10.

[32] J. Balach, J. Linnemann, T. Jaumann, L. Giebeler, *J. Mater. Chem. A* **2018**, *6*, 23127.

[33] C. Y. Zhang, X. Lu, X. Han, J. Yu, C. Zhang, C. Huang, L. Balcells, A. G. Manjón, J. Jacas Biendicho, J. Li, J. Arbiol, G. Sun, J. Y. Zhou, A. Cabot, *J. Am. Chem. Soc.* **2023**, *145*, 18992.

[34] J. Yu, C. Huang, O. Usoltsev, A. P. Black, K. Gupta, M. C. Spadaro, I. Pinto-Huguet, M. Botifoll, C. Li, J. Herrero-Martín, J. Zhou, A. Ponrouch, R. Zhao, L. Balcells, C. Y. Zhang, A. Cabot, J. Arbiol, *ACS Nano* **2024**, *18*, 19268.

[35] C. Huang, J. Yu, C. Y. Zhang, Z. Cui, J. Chen, W. H. Lai, Y. J. Lei, B. Nan, X. Lu, R. He, L. Gong, J. Li, C. Li, X. Qi, Q. Xue, J. Y. Zhou, X. Qi, L. Balcells, J. Arbiol, A. Cabot, *Adv. Mater.* **2024**, *36*, 2400810.

[36] Q. Li, Z. Ma, M. Liu, Y. Jiang, M. Fu, Y. Fan, X. Qin, A. Song, G. Shao, Y. Xu, *Angew. Chem., Int. Ed.* **2024**, *64*, 202416176.

[37] L. Lin, P. Su, Y. Han, Y. Xu, Q. Ni, X. Zhang, P. Xiong, Z. Sun, G. Sun, X. Chen, *Science* **2024**, *5*, 100264.

[38] T. Li, Y. Sun, K. Shi, W. Qin, H. Chen, J. Li, Y. Zheng, Q. Liu, Z. Liang, *AIChE J.* **2024**, *70*, 18327.

[39] K. Adachi, K. Sato, M. Takeda, *J. Phys. Soc. Japan* **1969**, *26*, 631.

[40] Z. Wang, J. Li, X. Tian, X. Wang, Y. Yu, K. A. Owusu, L. He, L. Mai, *ACS Appl. Mater. Interfaces* **2016**, *8*, 19386.

[41] X. Xu, F. Song, S. Hu, *Nat. Commun.* **2016**, *7*, 12324.

[42] J. Li, C. Xing, Y. Zhang, T. Zhang, M. C. Spadaro, Q. Wu, Y. Yi, S. He, J. Llorca, J. Arbiol, A. Cabot, C. Cui, *Small* **2021**, *17*, 2006623.

[43] J. Li, Y. Ma, J. Yu, L. Li, H. Yang, W. Gu, J. Shi, J. Wang, Y. Zhu, *ChemSusChem* **2024**, *18*, 202401098.

[44] Y. Ma, L. Li, J. Tang, Z. Hu, Y. Zhang, H. Ge, N. Jian, J. Zhao, A. Cabot, J. Li, *J. Mater. Chem. A* **2024**, *12*, 33917.

[45] Y. Zhang, R. Liu, Y. Ma, N. Jian, H. Pan, Y. Liu, J. Deng, L. Li, Q. Shao, C. Li, J. Li, *J. Mater. Chem. A* **2024**, *12*, 17252.

[46] Y. Liu, X. Liu, Q. Feng, D. He, L. Zhang, C. Lian, R. Shen, G. Zhao, Y. Ji, D. Wang, G. Zhou, Y. Li, *Adv. Mater.* **2016**, *28*, 4747.

[47] C. Zhang, J. J. Biendicho, T. Zhang, R. Du, J. Li, X. Yang, J. Arbiol, Y. Zhou, J. R. Morante, A. Cabot, *Adv. Funct. Mater.* **2019**, *29*, 1903842.

[48] M. Li, Y. Li, Q. Cu, Y. Li, H. Li, Z. Li, M. Li, H. Liao, G. Li, G. Li, X. Wang, *Energy Mater. Adv.* **2023**, *4*, https://doi.org/10.34133/energymatadv.003.

[49] Y. Zhang, C. Kang, W. Zhao, Y. Song, J. Zhu, H. Huo, Y. Ma, C. Du, P. Zuo, S. Lou, G. Yin, *J. Am. Chem. Soc.* **2023**, *145*, 1728.

[50] Y. Wu, D. Li, J. Pan, Y. Sun, W. Huang, M. Wu, B. Zhang, F. Pan, K. Shi, Q. Liu, *J. Mater. Chem. A* **2022**, *10*, 16309.

[51] Z. W. Seh, Y. Sun, Q. Zhang, Y. Cui, *Chem. Soc. Rev.* **2016**, *45*, 5605.

[52] Q. Pang, X. Liang, C. Y. Kwok, L. F. Nazar, *Nat. Energy* **2016**, *1*, 16132.

[53] Z. Li, H. Bin Wu, X. W. Lou, *Energy Environ. Sci.* **2016**, *9*, 3061.

[54] M. Qu, Y. Bai, L. Peng, L. Wang, H. Li, Z. Wang, K. Sun, *Energy Storage Mater.* **2024**, *70*, 103439.

[55] Q. Cheng, W. Xu, S. Qin, S. Das, T. Jin, A. Li, A. C. Li, B. Qie, P. Yao, H. Zhai, C. Shi, X. Yong, Y. Yang, *Angew. Chem., Int. Ed.* **2019**, *58*, 5557.

[56] S. H. Chung, C. H. Chang, A. Manthiram, *Energy Environ. Sci.* **2016**, *9*, 3188.

[57] J. Zhang, C. You, H. Lin, J. Wang, *Energy Environ. Mater.* **2022**, *5*, 731.

[58] Y. Tsao, M. Lee, E. C. Miller, G. Gao, J. Park, S. Chen, T. Katsumata, H. Tran, L. W. Wang, M. F. Toney, Y. Cui, Z. Bao, *Joule* **2019**, *3*, 872.

[59] R. Xu, I. Belharouak, J. C. M. Li, X. Zhang, I. Bloom, J. Bareño, *Adv. Energy Mater.* **2013**, *3*, 833.

[60] Q. Qi, X. Lv, W. Lv, Q. H. Yang, *J. Energy Chem.* **2019**, *39*, 88.

[61] C. Xia, C. Y. Kwok, L. F. Nazar, *Science* **2018**, *361*, 777.

[62] H. Tian, F. Xin, X. Wang, W. He, W. Han, *J. Mater.* **2015**, *1*, 153.

[63] H. Lin, S. Zhang, T. Zhang, S. Cao, H. Ye, Q. Yao, G. W. Zheng, J. Y. Lee, *ACS Nano* **2019**, *13*, 7073.

[64] L. Fu, D. Liu, X. Zuo, H. Yu, Z. Fu, Y. Zhang, *Sci. China Mater.* **2023**, *66*, 4587.

[65] R. Ciancio, R. E. Dunin-Borkowski, E. Snoeck, M. Kociak, R. Holmestad, J. Verbeeck, A. I. Kirkland, G. Kothleitner, J. Arbiol, *Microsc. Microanal.* **2022**, *28*, 2900.